Journal of Materials Chemistry A

Accepted Manuscript

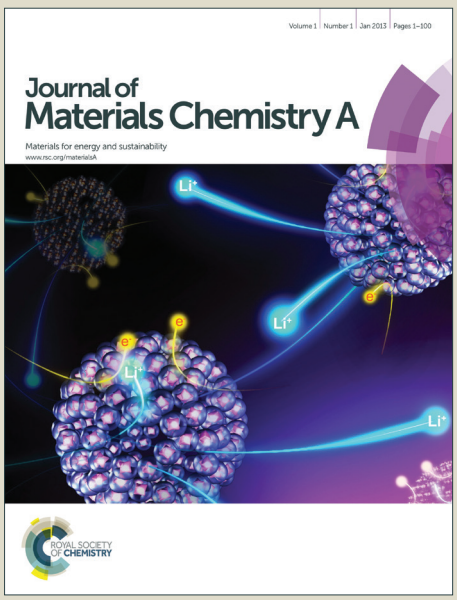

ROYAL SOCIETY OF CHEMISTRY

www.rsc.org/materialsA

Low activation energies for interstitial oxygen conduction in the layered perovskites $La_{1+x}Sr_{1-x}InO_{4+\delta}$

L. Troncoso[a], J.A. Alonso[a], A. Aguadero[b]

[a]*Instituto de Ciencia de Materiales de Madrid, CSIC, Cantoblanco, 28049 Madrid, Spain*

[b]*Department of Materials, Imperial College London, London, United Kingdom SW7 AZ*

Abstract

K_2NiF_4-type $La_{1+x}Sr_{1-x}InO_{4+\delta}$ (x= 0.1, 0.2) oxides have been prepared and investigated as possible solid electrolytes for solid-oxide fuel cells (SOFC). These materials were synthesized using a citrate-nitrate soft-chemistry technique followed by annealings in air at temperatures of 1000ºC. Preliminary characterization by x-ray diffraction (XRD) indicated that these layered perovskites crystallize in an orthorhombic structure with space group *Pbca*. The crystal structural features were explored at RT by neutron powder diffraction (NPD). The capability of incorporating interstitial oxygen atoms (δ) and their effect on the crystal structure were identified by difference Fourier maps in the NaCl layers of the K_2NiF_4 structure; subsequent Rietveld refinements yielded excess oxygen values, δ= 0.07(1) and 0.11(2) for x= 0.1 and 0.2, respectively. The electrical properties were studied by impedance spectroscopy (IS) in the temperature range 500–900 °C and compared with those of the parent compound $LaSrInO_4$. A better conductivity was observed for $La_{1.2}Sr_{0.8}InO_{4.11}$, which is consistent with the higher quantity of interstitial oxygen found from NPD data. The extremely low activation energy of only 0.51 eV for the conduction mechanism via interstitials at low temperatures (T< 650ºC) is significantly smaller than those of other electrolytes working with a vacancy mechanism, typically of 1 eV, as theoretically predicted. The present result endorses the validity of this design procedure and supports K_2NiF_4-related compounds as promising candidates for solid-oxide electrolytes.

Keywords: Neutron powder diffraction; Layered perovskite; Rietveld analysis

*Corresponding author. E-mail: ja.alonso@icmm.csic.es

1. Introduction

Solid-oxide fuel cells (SOFC) are electrochemical devices that transform the fuel energy directly into electricity. They are constituted by ceramics oxides, included the solid electrolytes, which in general entail high operation temperatures (about 1000ºC) to promote the charge carriers mobility. The development of intermediate temperature SOFC (working between 500-800ºC) necessarily requires new electrolyte materials able to conduct O^{2-} ions with lower activation energies, so as to decrease the electrical resistance and to improve the electrochemical kinetics.

Solid electrolytes for solid-oxide fuel cells conduct electricity through the movement of oxygen ions. Typical commercially available materials are YSZ [1] or GDC [2] (with compositions $Zr_{1-x}Y_xO_{2-\delta}$ or $Ce_{1-x}GdO_{2-\delta}$ and defect fluorite structure), displaying a high oxide-ion conduction above 700°C. Instead fluorite, many perovskite-type oxides showing oxygen sub-stoichiometry (allowing an oxygen-vacancy conduction mechanism) have been explored, some of them finding applications as solid electrolytes, like those based upon $LaGaO_3$ system (with composition $La_{1-x}Sr_xGa_{1-y}Mg_yO_{3-\delta}$, known as LSGM materials) [3-6], $LaMO_3$ perovskite oxides (M = Al, Sc, In, and rare-earth ions) [7] and Ruddlesden–Popper type compounds $AO(ABO_3)n$ (n=1, 2, 3) [8-10].

Instead of three-dimensional perovskite structures, there are reports on layered perovskite-type compounds with K_2NiF_4 structure that are well known to incorporate interstitial oxygen atoms inside their frameworks [11-13]. In particular, layered perovskites containing Al, In and Zr with K_2NiF_4-type structure, like $LaSrAlO_4$ [14-16], have originated great interest by its notable transport properties since they are able to simultaneously exhibit oxygen vacancies and interstitial oxygen atoms in the structural framework [17]. The structure of this type of compounds with nominal stoichiometry $A_2BO_{4+\delta}$ is constituted by BO_6 octahedra that share vertices in a single perovskite layer, which alternates with a NaCl-type structure concerning AO layers. In an ideal lattice, BO_6 octahedra are corner-linked by equatorials O1 oxygen atoms, while the axial O2 oxygens link together each perovskite layer with the adjacent NaCl layers [18-19]. Extra

oxygen atoms (δ) are accommodated into the NaCl layer, where there is room for interstitial O^{2-} ions. The wide range of non-stoichiometry that are able to incorporate these materials make them especially attractive for its use as electrolytes in solid-oxide fuel cells.

In the present work we describe the synthesis and characterization of a new family of oxides of composition $La_{1+x}Sr_{1-x}InO_{4+\delta}$. The parent compound is $LaSrInO_4$, where some divalent Sr is replaced by trivalent La ions, thus driving the incorporation of some extra oxygen atoms (nominally $\delta = x/2$) to maintain the electroneutrality of the crystal. The present characterization includes the evaluation of the *ac* electric conductivity and a neutron diffraction study, useful to locate the positions and determine the occupation of the interstitial oxygen atoms.

2. Experimental

$La_{1+x}Sr_{1-x}InO_{4+\delta}$ (x= 0, 0.1, 0.2) oxides were prepared via a nitrate-citrate route; the x= 0 compound was also prepared as a reference. Stoichiometric amounts of analytical grade $Sr(NO_3)_2$, La_2O_3 and $In(NO_3).9H_2O$ were dissolved under stirring in 250 ml of 10 % citric-acid aqueous solution with several droplets of concentrated HNO_3. This mixture was slowly evaporated, leading to organic resins where a random distribution of the involved cations is expected. The resins were dried at 120 ºC and slowly decomposed at temperatures up to 600 ºC. A subsequent treatment at 800 ºC for 2 h ensures the total elimination of all the organic materials and nitrates. A final heating at 1000ºC for 12 h gave rise to well crystallized, homogeneous samples.

The identification and characterization of the final products were carried out by X-ray diffraction (XRD) for phase identification and to asses phase purity using a Bruker-axs D8 diffractometer (40 kV, 30 mA), controlled by a DIFFRACTplus software, in Bragg-Brentano reflection geometry with CuKα radiation (λ = 1.5418 Å). Neutron powder diffraction (NPD) data were collected at the HRPT diffractometer of SINQ spallation source (Paul Scherrer Institute, Villigen, Switzerland) with a wavelength of 1.494 Å. 2 g of each sample were contained in a vanadium can during the data acquisition at RT,

which lasted 2 h. The crystal structures were analyzed by the Rietveld method [20], using the FULLPROF refinement program [21]. The peak profiles were modeled by a pseudo-Voigt function. The following parameters were refined in the final runs: scale factor, background coefficients, zero-point error, pseudo-Voigt corrected for asymmetry parameters, unit-cell parameters, positional, isotropic thermal factors for the metals and anisotropic for O1 and O2 oxygen atoms. Occupancy factors for oxygen atoms were also refined for NPD data. The coherent scattering lengths for La, Sr, In and O were 8.240, 7.020, 4.065 and 5.803 fm, respectively.

For the electrical conductivity measurements, dense compounds are required. The prepared powders were pressed into pellets (7 mm in diameter and 1.4 mm thick) at 200 MPa during 5 min to form a green pellet. Then, these pellets were sintered in air at 1200 °C for 12 h. The final densities were in the range of 90–95%. Both sides of the pellets were painted with Pt paste, as current collectors and fired at 800°C for 1 hour. Ac conductivity was obtained by impedance spectroscopy. All the impedance measurements were performed in the 500–900 °C temperature range in air atmosphere. The impedance spectra were collected in an AUTOLAB system (PGSTAT30 and FRA2 module) from Eco Chemie B.V. The measurements were performed from 1 MHz to 100 mHz at open circuit using two electrode configurations with a signal amplitude of 50 mV. The experimental data were adjusted with the Zview program [22].
The densities of the pellets were determined using equation 1 and 2:

$$\varphi = \frac{m}{V} \tag{1}$$

and

$$\varphi_x = \frac{Z \cdot W}{V \cdot N_{avog}} \tag{2}$$

where φ and φ_x are the experimental and theoretical density of the sample, respectively.

The % of the degree of densification for the pellets is obtained as (φ/φ_x)x100.

3. Results and discussion

3.1. Crystal structure: X-ray and neutron powder diffraction studies

$La_{1+x}Sr_{1-x}InO_{4+\delta}$ (x= 0, 0.1, 0.2) samples were obtained as white, well-crystallized powders. Fig.1 displays the XRD patterns; they are characteristic of K_2NiF_4 structure for all the samples, indexed with orthorhombic symmetry. The crystal structures were refined at RT from NPD data in the P*bca* space group (No 61) as proposed by Titov [23] for the nominal composition $LaSrInO_4$. A minor impurity phase of $Sr_3La_4O_9$ was detected in the x>0 NPD patterns, and included in the refinements as a second phase. The percentage was determined by Rietveld analysis, giving 7.8(1)% and 9.2(7)% for x= 0.1 and 0.2, respectively. In the P*bca* model, La and Sr atoms are located at random at 8*c* (x,y,z) positions; In is placed at 4*b* (1/2,0,0) sites and the two types of oxygen atoms O1 and O2 are also at 8*c* sites. The presence of vacancies at the octahedral lattice are discarded, since the occupancy factors of O1 and O2 atoms yielded full stoichiometry for both positions. Difference Fourier maps (Fig. 2) allowed identifying the interstitial O3 oxygen atoms as conspicuous peaks of positive scattering density, placed at 8*c* Wyckoff sites with x≈y≈z≈0.25 positions and located at the NaCl layers.

After inclusion of this O3 atom in the structural model, the refinement of the occupancy factor gave δ= 0.07(1) and 0.11(2) for x= 0.1 and 0.2, respectively, slightly higher than the theoretical values. Fig. 3 illustrates the quality of the Rietveld fit for $La_{1-x}Sr_{1+x}InO_{4+\delta}$ (x= 0, 0.1, 0.2). Table 1 contains the main atomic parameters after the refinement. The displacement factors for O1 and O2 oxygen atoms were refined anisotropically. These values are listed in Table 2. The higher displacement factors for the oxygen atoms in the La^{3+}-rich samples may be a result of the disorder induced by the introduction of interstitial oxygen atoms. Table 3 includes some selected interatomic distances and bond angles.

The unit-cell volume subtly decreases when Sr is replaced by La (Table 1) since Sr^{2+} (ionic radius 1.18 Å in octahedral coordination) is fairly larger in size than La^{3+} (ionic radius 1.032 Å) [24]. (La,Sr)–O1 and (La,Sr)–O2 bond lengths are not highly influenced by this replacement. In fact, *a* unit-cell parameter tends to increase whereas c decreases, as a result of competing effects in the structure; the expansion of the *a* parameter may be a consequence of the repulsion of the extra O^{2-} ions located at the

NaCl layer, whereas the shrink along c is a purely steric effect when Sr^{2+} is replaced by smaller La^{3+} ions. Taking into account that the oxygen mobility in these materials has been reported to be anisotropic with the majority of the conductivity taking place in the *ab* plane [25], this expansion may have very important and interesting effects in the oxygen transport properties of these materials.

The evolution of the <In - O> distances (2.155(1) Å, 2.157(2) Å and 2.162(2) Å for x= 0.0, 0.1 and 0.2 respectively) is also determined by the compromise between the mentioned factors, first leading to a decrease (steric factor) and then to an increase of the In-O bond-lengths. As the amount of extra O3 ions increases and the stoichiometry reaches $\delta \approx 0.1$, the In-O2 axial distances noticeably increase indicating a weakening of the In-O bonds of the octahedra, driven by a shift of the electron cloud via O3-La-O2-In paths. The decrease of the average <La/Sr-O> distances is also related to this effect.

Fig. 4 shows a view of the orthorhombic crystal structure, consisting of layers of rotated InO_6 octahedra alternating with (La/Sr)-O layers with NaCl structure. The InO_6 octahedra are significantly tilted by 12.16°, 11.80° and 12.23° for x= 0.0, 0.1 and 0.2, respectively. The interstitial O3 atoms occupying the NaCl layer are bonded to (La,Sr) with reasonable distances of 2.562(2) Å and 2.560(2) Å in average for x= 0.1 and 0.2 respectively. Fig. 4 also displays the displacement ellipsoids for O1 and O2. It is noteworthy that the ellipsoids are flattened perpendicularly to the chemical bond, indicating an increased degree of freedom in these directions; also the axial O2 oxygens exhibit larger ellipsoids, since the chemical bonds to La/Sr are less covalent than those existing on the bc plane of the type In-O-In.

3.2. Ac measurements

The electrical properties of sintered pellets of $La_{1+x}Sr_{1-x}InO_4$ were assessed by means of *ac* impedance spectroscopy. Fig. 5 illustrates the impedance diagrams of $La_{1+x}Sr_{1-x}InO_{4+\delta}$ (x= 0.1, 0.2) compared to $LaSrInO_4$ measured in air at 600 °C. In general, all the measured spectra show two depressed arcs that contribute to the impedance spectrum; except for the diagram obtained at 800 °C and 900 ºC for x= 0.2, in which it

can only be distinguishable one arc (not shown). In Fig. 5 the presence of two arcs at 600ºC indicates that at least two processes contributed to the electrical properties. The low-frequencies arc has much lower size than the high frequency one. The amplitude of this arc increases slightly as increasing the temperature.

The spectra were fitted to equivalent circuits consisting of sub-circuits representing the bulk *(B)* plus the grain boundary *(gb)* and the electrode interface *(int)* (electrolyte and Pt electrode faces) performance (inset of Fig. 5). The sub-circuits consist of (R_{B+gb}-C_{B+gb})(R_{int}-C_{int}) where two series connected elements (*R*-*C*) describe the two observed processes that contribute to the impedance of the electrolyte. The first component (R_{B+gb}-C_{B+gb}) appears as a semi-circle at the high-frequency region. Although the bulk and grain boundary present different transport phenomena, it is not always possible to separate both processes. In fact, several times (for certain values of the resistance), it is not possible at all. We have fitted our data to the described model and we got the expected capacitances for the bulk+grain boundary contribution of around 10^{-9} to 10^{-11} F/cm. The second arc (R_{int}-C_{int}) we identified is a semi-circle at the low-frequency region and it represents the electrode interface with our materials. Here the capacitances are all lower than 10^{-7} F/cm.

All the values obtained that contribute to the electrolyte process (bulk+grain boundary) were normalized to the area and thickness of the pellets, for their subsequent comparison, thus the units for this representation are (Ω cm) for the resistances, R_{B+gb}, and (F/cm) for the capacitances, C_{B+gb}. In the case of the interfacial region (Pt//electrolyte//Pt), the term used to describe all the resistances associated with the Pt–electrolyte interface in the process, named as R_{int}, is the area specific resistance, ASR [26]. Here, we normalized by the superficial area, so the ASR parameters obtained in the fitting for each process were divided by two and the C_{int} values multiplied by two to consider the contribution of the two Pt electrodes. Thus the units for this representation are (Ω cm^2) for the resistances and (F/cm^2) for the capacitances. The units in Fig. 5 are given in (Ω cm) to represent the processes that occur inside the electrolyte.

Table 4 summarizes the fitting parameters for the impedance spectrum as a function of temperature for $La_{1+x}Sr_{1-x}InO_{4+\delta}$ (x= 0.1, 0.2) compared to $LaSrInO_4$ in air, as well as the values of the area-specific resistance. It can be seen that the resistances (R_{B+gb}, R_{int}) associated with the kinetics inside the electrolytes and the electrode processes decrease with increasing temperature, as expected.

According to the capacitance values obtained, the first arc may be related to the process that occurs inside the bulk and the grain boundary *(B+gb)*, and the second arc with the phenomena related to the transfer of charge between the materials and the electrodes *(int)*. It can be seen that the doped samples with interstitial oxygens inside the structure exhibit considerably lower impedance values than $LaSrInO_4$, especially for $La_{1.2}Sr_{0.8}InO_4$ sample, containing the highest amount of interstitial oxygen.

Fig. 6 shows the thermal variation of conductivity (σ) in air for $La_{1+x}Sr_{1-x}InO_{4+\delta}$ (x= 0.0, 0.1, 0.2), indicating a thermally activated conduction. The activation energy was calculated from Eq. 3, where E_a, σ_o and k are the activation energy, pre-exponential factor and Boltzmann constant, respectively.

$$\log(\sigma T) = \log \sigma_o - \frac{E_a}{kT} \quad (3)$$

We can observe for $La_{1.2}Sr_{0.8}InO_{4+\delta}$ two different trends in the conductivity, which have been fitted in two temperature regions. At low temperatures (500ºC≤T≤650ºC), $La_{1.2}Sr_{0.8}InO_{4+\delta}$ layered perovskite presents the lowest activation energy, E_a = 0.51 eV, (Fig. 6). At high temperatures (650ºC≤T≤900ºC), the value of the activation energy is 0.94 eV. For $La_{1+x}Sr_{1-x}InO_{4+\delta}$ (x= 0.0 and 0.1), Ea= 1.10 eV and 0.98 eV, respectively.

The improvement of the conductivity with the increasing amount of La is concomitant to the incorporation of interstitial oxide ions that compensates the increment of charge in the A site as Sr^{2+} is replaced by La^{3+}. The conductivity of O^{2-} oxide is improved by one order of magnitude for $La_{1.2}Sr_{0.8}InO_{4.1}$ at 900ºC with respect to the parent

compound. This is still far from the best values of conductivity of state-of-the-art O^{2-} ionic conductors. For the sake of comparison, Fig. 7 includes the conductivity of $La_{1.2}Sr_{0.8}InO_{4.11}$ together with those of typical electrolytes, namely YSZ, CGO and LSGM (taken from [26]). It can be seen that at high temperatures these electrolytes overcome the K_2NiF_4 system by several orders of magnitude, but at low temperatures $La_{1.2}Sr_{0.8}InO_{4.11}$ starts to be competitive. This is due to the extremely low activation energy of only 0.51 eV determined for this compound compared to those of YSZ, CGO y LSGM, typically of 1 eV [26]. This clearly shows that, when the conduction mechanism is via interstitials, the activation energy is much lower, as determined by simulation in $La_2CoO_{4+\delta}$ [27]. The present result endorses the validity of this design procedure and supports K_2NiF_4-related compounds as promising candidates for solid-oxide electrolytes.

4. Conclusions

The novel K_2NiF_4-type $La_{1+x}Sr_{1-x}InO_{4+\delta}$ (x= 0.1, 0.2) oxides have been successfully prepared via a nitrate-citrate route and studied by x-ray diffraction and neutron diffraction analysis in the P*bca* space group. It was possible to demonstrate that the crystal structure incorporates interstitial oxygen atoms (δ) in the NaCl layer as a consequence of the partial replacement of Sr^{2+} by La^{3+} ions; δ values of 0.07(1) and 0.11(2) are obtained for x= 0.1 and 0.2 respectively. In order to evaluate these layered perovskites as potential ion conductors, the conductivity of these oxides was determined by *ac* impedance spectroscopy and compared with that of $LaSrInO_4$ parent oxide. A lower activation energy and better conductivity (by an order of magnitude with respect to the parent compound) was observed for $La_{1.2}Sr_{0.8}InO_{4+0.11}$, which is consistent with the substantial amount of interstitial oxygens observed by NPD data and makes possible an easier movement of interstitial atoms in the expanded *ab* plane. An interstitial diffusion mechanism for O^{2-} ions is conceivable for these layered perovskite oxides, characterized by an extremely low activation energy for the O^{2-} motion via interstitial mechanism, of 0.51 eV in the low-temperatures region (500≤T≤650ºC).

Acknowledgments. We are grateful to the Spanish Ministry of Economy and Competitivity for granting the project MAT2013-41099-R, and ILL and PSI for making all facilities available for the neutron diffraction experiments. L.T. thanks the financial support of CONICYT for " Becas de Postdoctorado en el Extranjero BECAS CHILE ". AA wants to thank the European Commission for a Marie Curie IE fellowship.

References

[1] S.P.S. Badwal, Solid State lonics 52 (1992) 23

[2] B.C.H. Steele, Solid State Ionics 129 (2000) 95

[3] T. Ishihara, H. Matsuda and Y. Takata, J. Am. Chem. Soc., 116 (1994) 3801

[4] M. Feng and J. B. Goodenough, Eur. J. Solid State Inorg. Chem., T31 (1994) 663

[5] K. Huang, R. S. Tichy, J. B. Goodenough and C. Milliken, J. Am. Ceram. Soc., 81 (1998) 2581.

[6] S. Tao, J. T. S. Irvine and J. A. Kilner, Adv. Mater., 17 (2005) 1734.

[7] Hye-Lim Kim, Shin Kim, Kyu-Hyung Lee, Hong-Lim Lee, Ki-Tae Lee, Journal of Power Sources 267 (2014) 723

[8] I. Kagomiy, K. Jimbo, K.-I. Kakimoto, J. Sol. State Chem. 207 (2013) 184

[9]Y. Arachi, T. Asai, O. Yamamoto, Y. Takeda, N. Imanishi, Solid State Ionics 135 (2000) 757

[10] P.S. Anderson, F.M.B. Marques, D.C. Sinclair, A.R. West, Solid State Ionics 118 (1999) 229

[11] A. Aguadero, J.A. Alonso, M.J. Escudero, L. Daza, Solid State Ionics, 179 (2008) 393

[12] A. Aguadero, M. Pérez, J.A. Alonso, L. Daza, Journal of Power Sources, 151 (2005) 52

[13] A. Aguadero, J.A. Alonso, M.T. Fernández-Díaz, M.J. Escudero, L. Daza, J. Power Sources, 169 (2007) 17

[14] A. Novosselov, A. Pajaczkowska, E. Talik, Cryst. Res. Technol., 36 (2001) 859

[15] E. S. Raj, S. J. Skinner, J.A. Kilner, Solid State Sciences, 6 (2004) 825

[16] X.Q. Liu, X.M. Chen, Y. Xiao, Mat. Sci. and Engineering: B, 103 (2003) 276

[17]S. Kato, M. Ogasawara, M. Sugai, S. Nakata, Solid State Ionics, 149 (2002) 53

[18] S. F. Matara, G. Demazeaua, N. Ouainib, Solid State Sciences, 13 (2011) 1396

[19] L.-.G. Liu, Phys. Earth and Planetary Interiors, 17 (1978) 29

[20] H.M. Rietveld, J. Appl. Crystallogr. 2 (1969) 65

[21] J. Rodríguez-Carvajal, Physica B, 192 (1993) 55

[22] D. Johnson, Zview Program, version 3.2b, Scribner Associates, Inc. Southern Pines, North Carolina, 1990, 2010

[23] Yu.A. Titov, N.M. Belyavina, V.Ya. Markiv, M.S. Slobodyanik, Ya.A. Krayevska, Dopov. Nats. Akad. Nauk. Ukr. (2009) 160

[24] R.D. Shannon, Acta Crystallogr. A32 (1976) 751

[25] J.M. Bassat, P. Odier, A. Villesuzanne, C. Marin, M. Pouchard, Solid State Ionics 167 (2004) 341

[26] A. Aguadero, J.A. Alonso, M.J. Escudero, L. Daza, Solid State Ionics 179 (2008) 393

Table 1. Structural parameters after the Rietveld refinement of for $La_{1+x}Sr_{1-x}InO_{4+\delta}$ (x= 0.0, 0.1 and 0.2) in the space group P*bca* from NPD data at RT.

	$LaSrInO_4$	**$La_{1.1}Sr_{0.9}InO_{4+\delta}$**	**$La_{1.2}Sr_{0.8}InO_{4+\delta}$**
a(Å)	12.6034(1)	12.6028(4)	12.6085(6)
b(Å)	5.8779(1)	5.8798 (2)	5.8789(3)
c(Å)	5.8394(1)	5.8352(2)	5.8338(3)
V(Å^3)	432.61(1)	432.40(2)	432.42(4)
La/Sr 8*c* (x,y,z)			
x	0.14540(4)	0.14570(7)	0.14575 (8)
y	-0.01333(12)	-0.01370(18)	-0.0155(2)
z	0.96951(12)	0.96904(18)	0.9726(2)
B(Å^2)	0.56(3)	1.02 (4)	1.14(5)
focc	0.49(1)/0.51(1)	0.56(1)/0.44(1)	0.59(1)/0.41(1)
In *4b (1/2 0 0)*			
B(Å^2)	0.39(6)	0.55(8)	0.69 (11)
Occ	0.50	0.50	0.50
O1 8*c*(x,y,z)			
x	0.0267(1)	0.0259(1)	0.0269(2)
y	0.2147(2)	0.2160(3)	0.2161(4)
z	0.2145(3)	0.2158(5)	0.2120(3)
focc	1.000	1.000	1.000
O2 8*c*(x,y,z)			
x	0.3274(1)	0.3265(1)	0.3268(1)
y	0.0763(2)	0.0779(3)	0.0807(2)
z	0.0267(2)	0.0259(4)	0.0301(3)
focc	1.000	1.000	1.000
O3 8*c*(x,y,z)			
x		0.221 (2)	0.216(1)
y		0.2912(5)	0.249(4)
z		0.206(5)	0.267(5)
B(Å^2)		1.32(5)	3.88(5)
focc		0.035(6)	0.054(1)
χ^2	1.92	1.25	2.80
R_p(%)	2.57	3.48	4.44
R_{wp}(%)	3.28	4.47	5.96
R_{Bragg}(%)	3.40	5.95	7.83

Table 2. Anisotropic displacement factors for O1 and O2 in $La_{1+x}Sr_{1-x}InO_{4+\delta}$ (x= 0.0, 0.1, 0.2) from NPD data at RT.

	$LaSrInO_4$	**$La_{1.1}Sr_{0.9}InO_{4+\delta}$**	**$La_{1.2}Sr_{0.8}InO_{4+\delta}$**
O1 8*c*(x,y,z)			
β_{11}	17.8(1)	24.7 (2)	26.3 (3)
β_{22}	28.3(6)	87.2 (8)	60.6(10)
β_{33}	42.7(6)	81.8 (8)	125.9(13)
β_{12}	-4.2(3)	-15.9 (3)	-27.4(5)
β_{13}	14.5(3)	11.4 (4)	5.0(5)
β_{23}	-33.8(2)	32.7 (8)	43.7(10)
O2 8*c*(x,y,z)			
β_{11}	3.6(1)	19.3(2)	16.4(2)
β_{22}	84.4(6)	103.3(7)	56.6(9)
β_{33}	173.6(8)	233.0(11)	262.3(15)
β_{12}	1.1(2)	15.4(3)	13.4(4)
β_{13}	-7.7(3)	1.7(4)	15.9(6)
β_{23}	30.2(6)	35.1(8)	20.0(11)

* Anisotropic Betas $\beta \times 10^{-4}$

Table 3. Main interatomic distances ($Å^2$) and angles (°) for $La_{1+x}Sr_{1-x}In_{4+\delta}$ (x= 0.0, 0.1 and 0.2) determined from NPD data at RT.

	$LaSrInO_4$	**$La_{1.1}Sr_{0.9}InO_4$**	**$La_{1.2}Sr_{0.8}InO_4$**
La/Sr-O1	2.466(4)	2.484(2)	2.468(2)
La/Sr-O1	2.695(2)	2.695(2)	2.695(2)
La/Sr-O1	2.745(4)	2.742(2)	2.767(2)
La/Sr-O2	2.377(1)	2.363(2)	2.366(2)
La/Sr-O2	2.634(4)	2.636(3)	2.636(3)
La/Sr-O2	2.459(2)	2.452(2)	2.425(2)
La/Sr-O3		2.508(17)	2.621(5)
La/Sr-O3		2.901(17)	2.694(4)
La/Sr-O3		2.459(16)	2.81(2)
La/Sr-O3		2.141(17)	2.15(2)
<La/Sr–O>*	**2.563(3)**	**2.562(2)**	**2.560(2)**
In-O1 (x2)	2.119(1)	2.117(2)	2.115(2)
In-O1 (x2)	2.118(2)	2.114(3)	2.122(2)
In-O2 (x2)	2.227(1)	2.240(2)	2.249(2)
<In–O>	**2.155(1)**	**2.157(2)**	**2.162(2)**
In-O1-In	155.69(5)	156.40(9)	155.55(8)

*Average <La/Sr-O> do not include distances to O3

Table 4. Parameters obtained from the data fitting of impedance measurements as a function of temperature for $La_{1+x}Sr_{1-x}In_{4+\delta}$ (x= 0.0, 0.1 and 0.2) in air under *ac* conditions and the area specific resistance (ASR). Conductivity values, σ_{B+gb}, are also given.

	$LaSrInO_4$	**$La_{1.1}Sr_{0.9}InO_4$**	**$La_{1.2}Sr_{0.8}InO_4$**
500°C			
R_{B+gb} (Ωcm)	$20.5(2) \times 10^5$	$28.2(2) \times 10^4$	$21.1(4) \times 10^4$
σ_{B+gb} (S/cm)	0.050(5)	$0.35(5) \times 10^{-4}$	$50(3) \times 10^{-4}$
C_{B+gb} (F/cm)	$19.5(2) \times 10^{-12}$	$11(3) \times 10^{-10}$	$0.73(1) \times 10^{-10}$
ASR (Ωcm²)		$0.79(3) \times 10^4$	$27(3) \times 10^4$
C_{int} (F/cm²)		$11.34(4) \times 10^{-6}$	$11.11(3) \times 10^{-4}$
600°C			
R_{B+gb} (Ωcm)	$37.6(2) \times 10^4$	$432(2) \times 10^4$	$11.58(1) \times 10^3$
σ_{B+gb} (S/cm)	0.27(1)	0.23(1)	$7(1) \times 10^{-2}$
C_{B+gb} (F/cm)	$76.3(1) \times 10^{-12}$	$12.79(4) \times 10^{-10}$	$4.52(4) \times 10^{-10}$
ASR (Ωcm²)		$0.65(10) \times 10^3$	$1.16(3) \times 10^2$
C_{int} (F/cm²)		$16.08(3) \times 10^{-5}$	$11.1(6) \times 10^{-4}$
700°C			
R_{B+gb} (Ωcm)	$8.7(0.2) \times 10^3$	$2.48(1) \times 10^4$	$5.72(1) \times 10^3$
σ_{B+gb} (S/cm)	0.12 (1)	0.4(1)	0.17(1)
C_{B+gb} (F/cm)	$69.5(2) \times 10^{-12}$	$62.4(1) \times 10^{-10}$	$3.8(1) \times 10^{-6}$
ASR (Ωcm²)		$0.2(1) \times 10^2$	$5(7) \times 10^2$
C_{int} (F/cm²)		$17.8(2) \times 10^{-5}$	$11.1(7) \times 10^{-4}$
800°C			
R_{B+gb} (Ωcm)	$218.2(0.2) \times 10^2$	$6.93(4) \times 10^3$	2061.66 (4)
σ_{B+gb} (S/cm)	0.05 (1)	$0.14(3) \times 10^{-3}$	$4.85(3) \times 10^{-4}$
C_{B+gb} (F/cm)	$76.3(2) \times 10^{-12}$	$2.57(1) \times 10^{-8}$	
ASR (Ωcm²)		$0.49(3) \times 10^2$	12.3(2)
C_{int} (F/cm²)		$17.5(1) \times 10^{-5}$	$9.9(3) \times 10^{-4}$
900°C			
R_{B+gb} (Ωcm)	$6.62(6) \times 10^3$	$4.1(4) \times 10^3$	925.7 (4)
σ_{B+gb} (S/cm)	0.15(2)	0.250(3)	$11(3) \times 10^{-4}$
C_{B+gb} (F/cm)	$8.3(1) \times 10^{-11}$	$15.8(1) \times 10^{-13}$	
ASR (Ωcm²)		27.7(1)	$7.4(3) \times 10^{-1}$
C_{int} (F/cm²)		$24.3(4) \times 10^{-5}$	$11.7(1) \times 10^{-4}$

Figure Captions

Figure 1. XRD patterns of $La_{1+x}Sr_{1-x}InO_{4+\delta}$ (x= 0.0, 0.1, 0.2) indexed in an orthorhombic unit cell (space group P*bca*).

Figure 2. Localization of the interstitial oxygen atoms (O3) by difference Fourier analysis, corresponding to z= 0.25 layer, from NPD data at RT.

Figure 3. Observed (crosses), calculated (full line) and difference (at the bottom) NPD profile for $La_{1+x}Sr_{1-x}InO_{4+\delta}$, a) x= 0.0, b) x= 0.1 and c) x= 0.2 at RT refined in the P*bca* space group. The vertical markers correspond to the allowed Bragg reflections for the main phase; the second series of markers correspond to $Sr_3La_4O_9$ minor impurity phase.

Figure 4. Crystal structure along the c direction of $La_{1.2}Sr_{0.8}InO_{4+\delta}$ showing sheets of tilted InO_6 octahedra alternating with (La,Sr)-O layers, where interstitial O3 oxygen atoms are located. Anisotropic ellipsoids for O1 and O2 oxygen atoms are also shown.

Figure 5. ac impedance spectra of $La_{1+x}Sr_{1-x}InO_{4+\delta}$ (x= 0, 0.1, 0.2) with Pt electrode at 600°C in air. The determination of the resistances was obtained with two series of RC parallel circuits proposed as the electrical equivalent circuit.

Figure 6. Thermal variation of conductivity (σ) versus 1000/T in air for $La_{1+x}Sr_{1-x}InO_{4+\delta}$ (x= 0.0, 0.1, 0.2)

Figure 7. Thermal variation of conductivity for various solid electrolytes (YSZ, CDO and LSGM) (from ref [26]) compared with that of $La_{1.2}Sr_{0.8}InO_{4.11}$, in air.

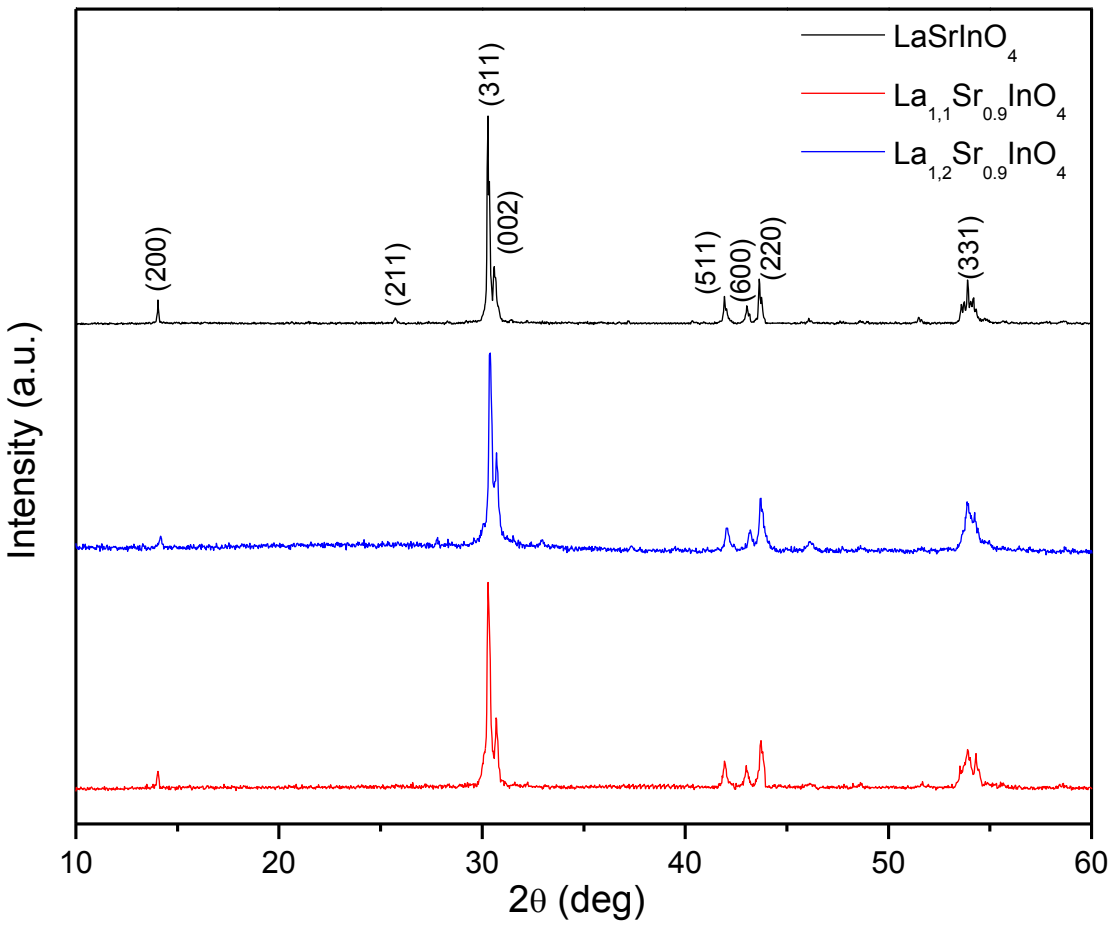

Figure 1

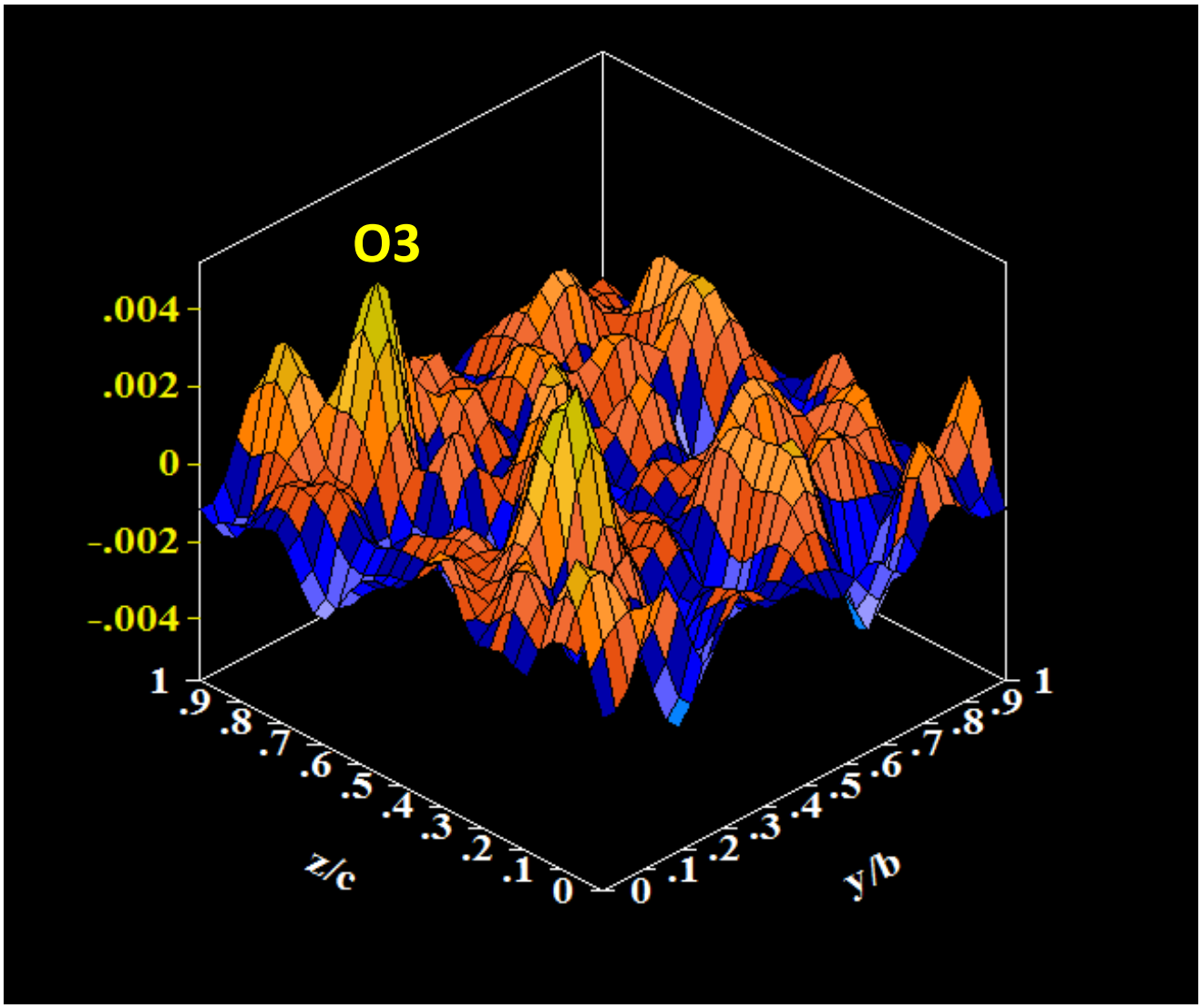

Figure 2

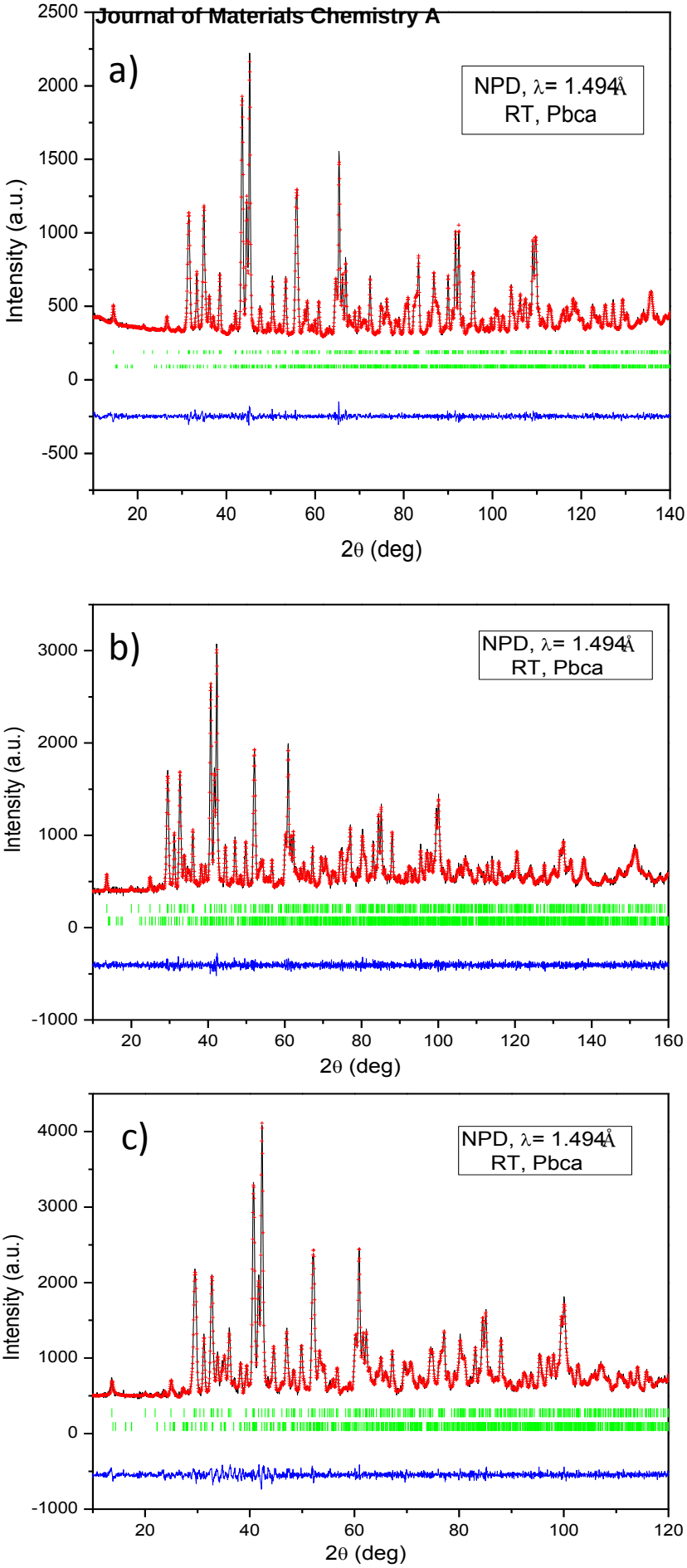

Figure 3

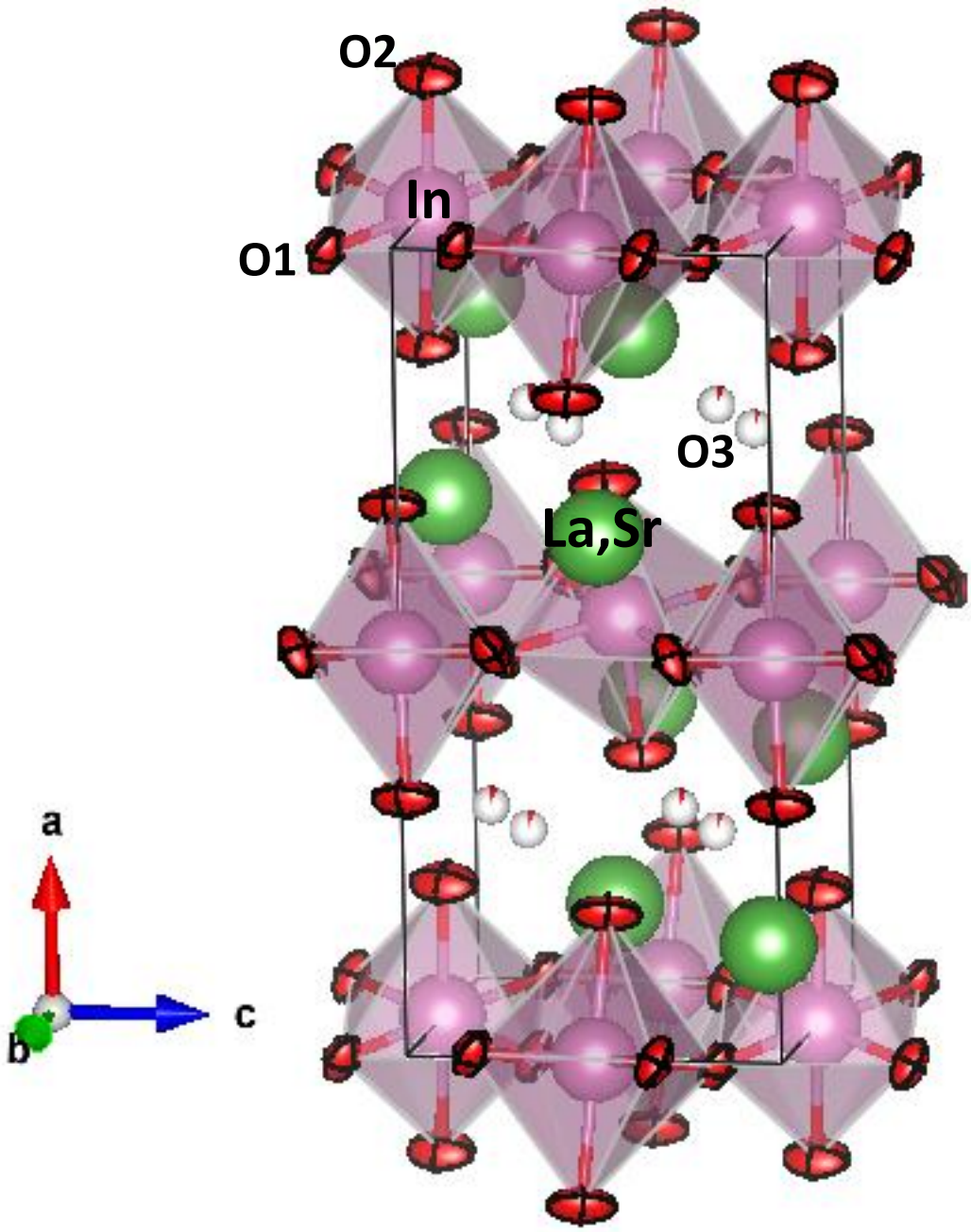

Figure 4

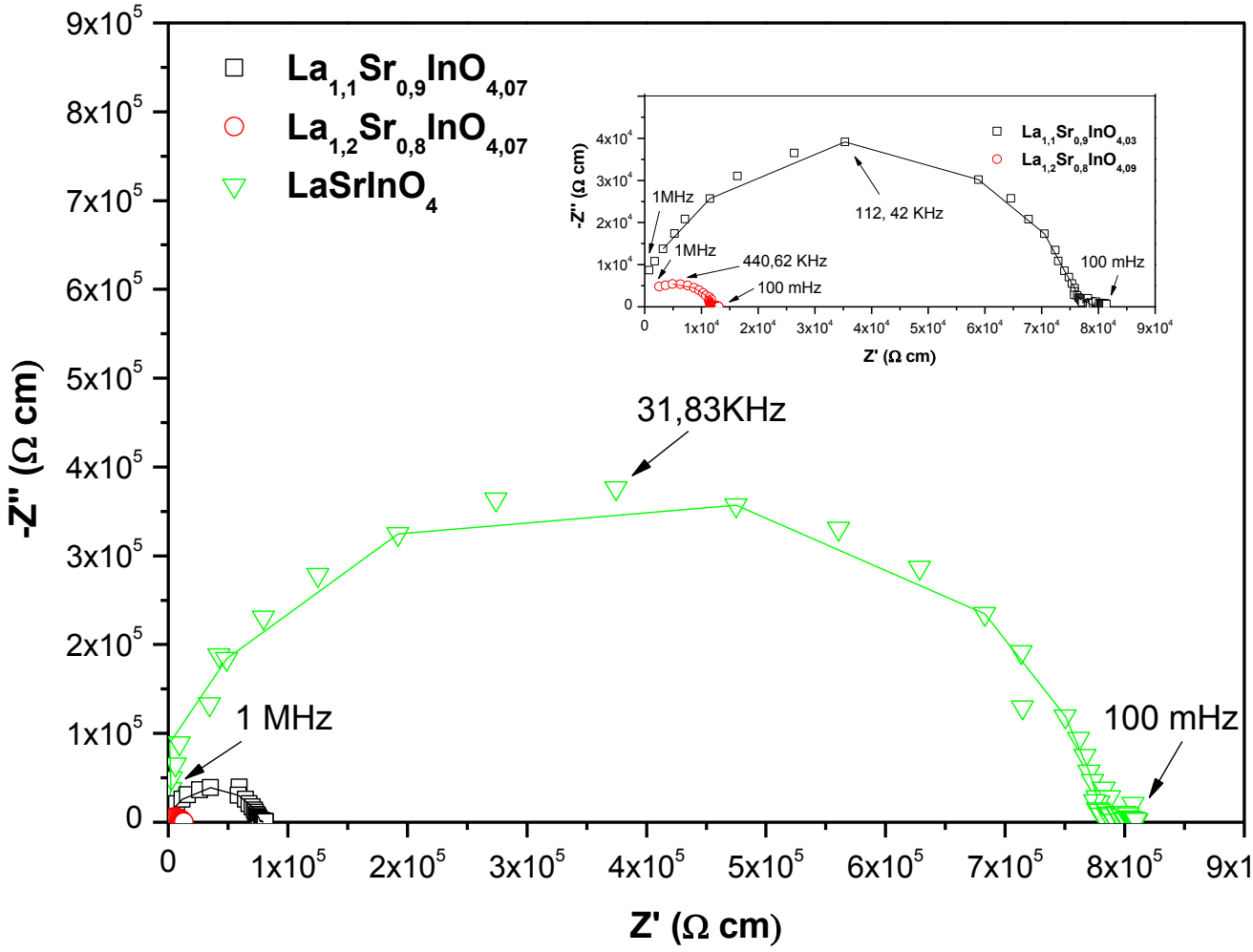

Figure 5

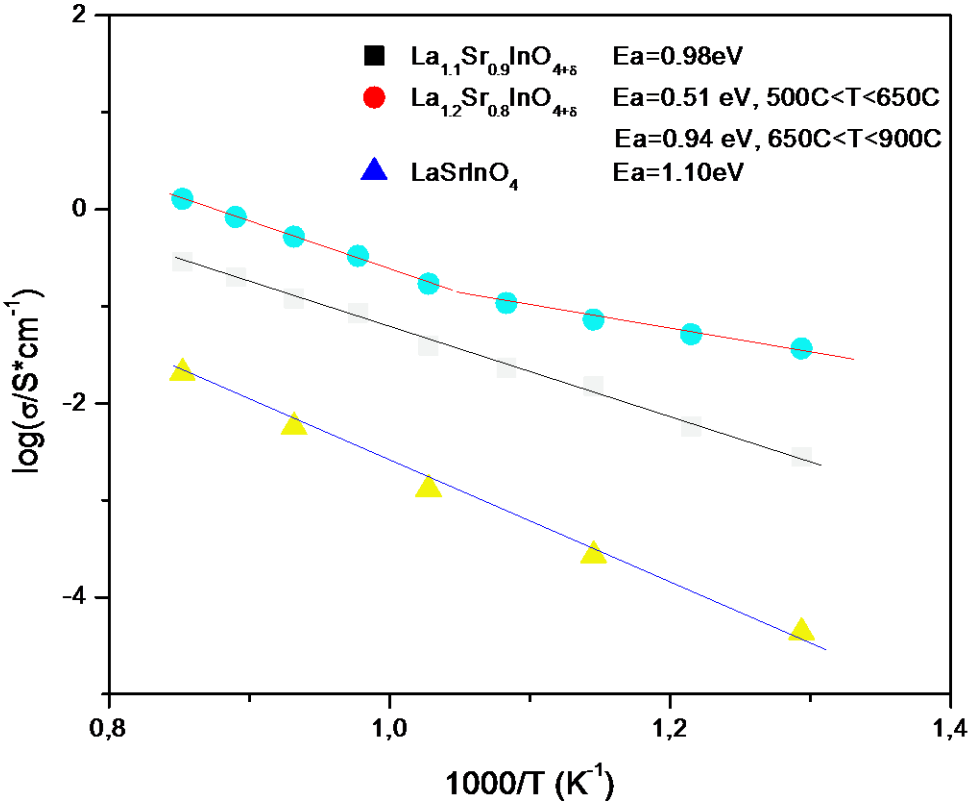

Figure 6

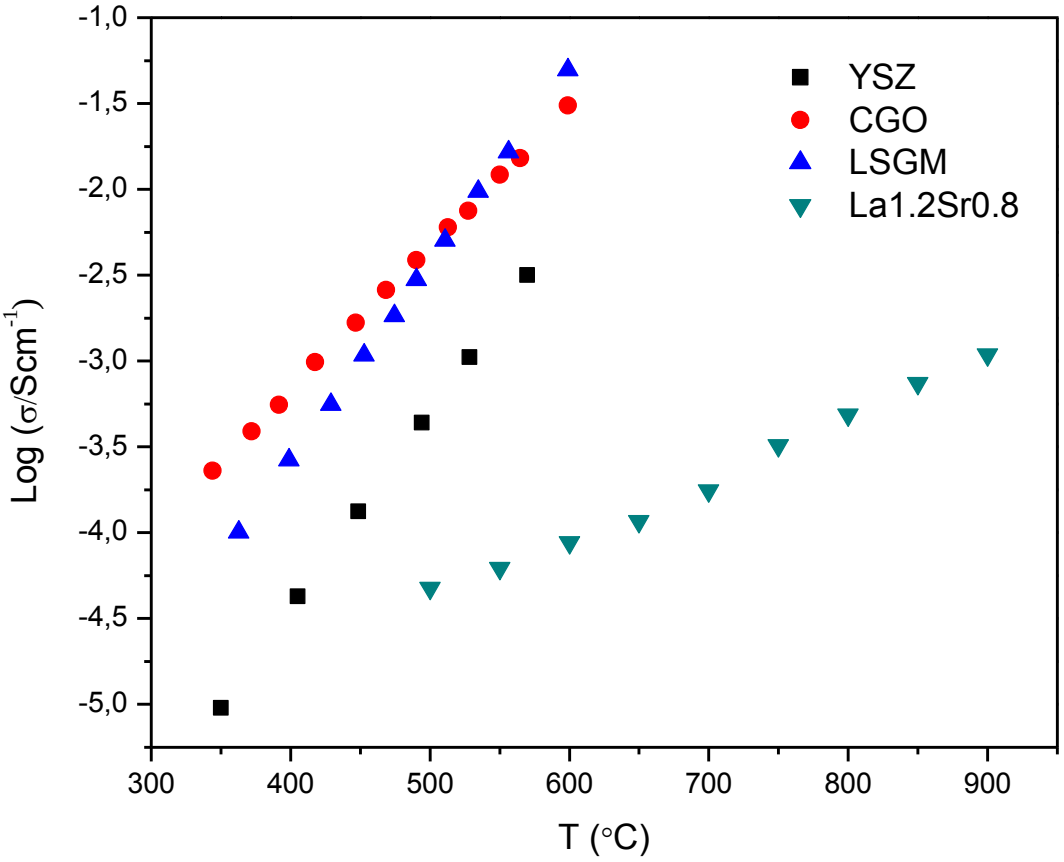

Figure 7

GRAPHICAL ABSTRACT

Low activation energies for interstitial oxygen conduction in the layered perovskites $La_{1+x}Sr_{1-x}InO_{4+\delta}$

L. Troncoso[a], J.A. Alonso[a],* A. Aguadero[b]

[a]*Instituto de Ciencia de Materiales de Madrid, CSIC, Cantoblanco, 28049 Madrid, Spain*

[b]*Department of Materials, Imperial College London, London, United Kingdom SW7 AZ*

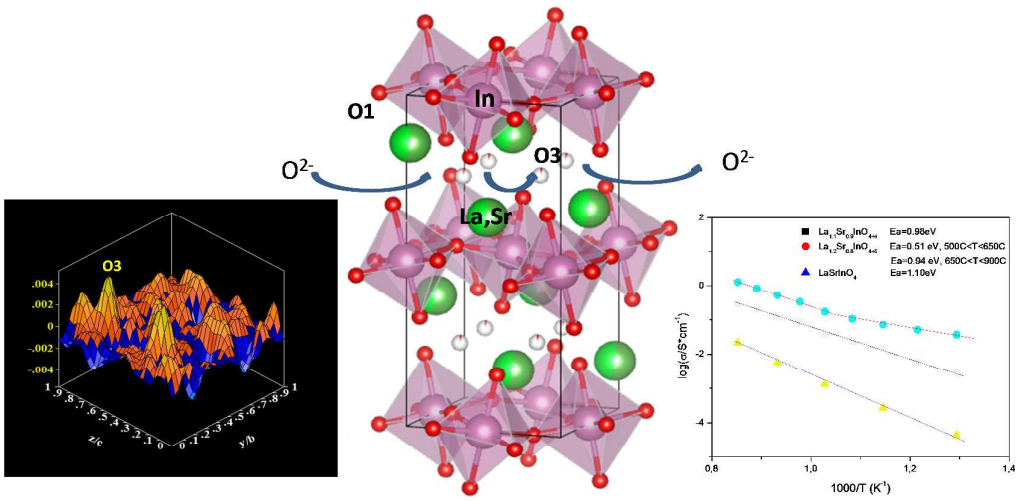

Interstitial oxygen atoms (δ), identified by difference Fourier maps from (NPD) data, enhance the conductivity for $La_{1.2}Sr_{0.8}InO_{4.11}$, with an extremely low activation energy of only 0.51 eV for this conduction mechanism of O^{2-} at low temperatures.